Analysis of Viscous Micropumps and Microturbines

David DeCourtye
Mihir Sen
Mohamed Gad-el-Hak

Department of Aerospace and Mechanical Engineering
University of Notre Dame
Notre Dame, IN 46556
U.S.A.

Manuscript number WH0254-R2 appeared in
International Journal Of Computational Fluid Dynamics, vol. **10**, pp. 13–25, 1998.

Abstract

A numerical study of the three-dimensional viscous fluid flow in a novel pump/turbine device appropriate for microscale applications is performed. The device essentially consists of a rotating or free-to-rotate cylinder eccentrically placed in a channel, and is shown to be capable of generating a net flow against an externally imposed pressure gradient, or, conversely, generating a net torque in the presence of an externally imposed bulk flow. Full Navier-Stokes, finite-element simulations are carried out to study the influence of the width and other geometric as well as dynamic parameters, and the results are compared to previous two-dimensional numerical and physical experiments. The three-dimensional simulations indicate a gradual decrease of the bulk velocity and pump performance as the two side walls become closer providing increased viscous resistance to the flow. However, effective pumping is still observed with extremely narrow channels. The utility of the device as a microturbine is also demonstrated for the first time in the present simulations. Particularly, the angular velocity of the rotor and the viscous torque are determined when a bulk velocity is imposed.

1 Introduction

Manufacturing processes that can create extremely small machines have been developed in recent years (Angell et al., 1983; Gabriel et al., 1988; Gabriel, 1995). Motors, electrostatic actuators, pneumatic actuators, valves, gears and tweezers of about 10 μm size have been fabricated. These have been used as sensors for pressure, temperature, velocity, mass flow, or sound, and as actuators for linear and angular motions. Current usage for microelectromechanical systems (MEMS) ranges from airbags to blood analysis (O'Connor, 1992; Hogan, 1996). There is considerable work under way to include other applications,

one example being the micro-steam engine described by Lipkin (1993). Many of these new applications will need fluid to be pumped in a duct; at such small scales this is a challenge (Gravesen et al., 1993).

There have been several studies of microfabricated pumps. Some of them use non-mechanical effects such as, for example, ion-drag in electrohydrodynamic pumps (Bart et al., 1990; Richter et al., 1991a; 1991b; Fuhr et al., 1992) and valveless pumping by ultrasound waves (Moroney et al., 1991). It is important to emphasize, however, that mechanical pumps based on conventional centrifugal or axial turbomachinery will not work at micromachine scales where the Reynolds numbers, Re, are typically small, of the order of 1 or less.[1] There, viscous forces dominate in relation to inertia. Centrifugal forces are negligible and, furthermore, the Kutta condition through which lift is normally generated is invalid when inertial forces are vanishingly small.

In general there are three ways in which mechanical micropumps can work at low Reynolds numbers: (1) Positive-displacement pumps (Van Lintel et al., 1988; Esashi et al., 1989; Smits,1990); (2) Continuous, parallel-axis, screw-type rotary pumps (Taylor, 1972); (3) Continuous, transverse-axis rotary pumps. The latter is the class of machines that is considered in here for both hauling fluids in small conduits and generating net torque and thus useful work as turbines.

It is possible to generate axial fluid motion in open channels through the rotation of a cylinder in a viscous fluid medium. Odell and Kovasznay (1971) studied a pump based on this principle at high Reynolds numbers. Sen et al. (1996) carried out an experimental study of a different version of such a pump more suited for low Re applications. The novel

[1] One could envision a class of micro-turbomachines having exceedingly high rpm. In that case, Re could be much higher than one. In fact, the micro-gas-turbine under development at MIT is such a device. The primary concern in this paper is, however, with turbomachines that have small size *and* modest rotational speed.

viscous pump consists simply of a transverse-axis cylindrical rotor eccentrically placed in a channel, so that the differential viscous resistance between the small and large gaps causes a net flow along the duct. The Reynolds numbers involved in Sen et al.'s work were low ($0.01 \leq Re \leq 10$), typical of microscale devices, but achieved using a macroscale rotor and a very viscous fluid. The bulk velocities obtained were as high as 10% of the surface speed of the rotating cylinder. A finite-element solution for low-Reynolds-number, uniform, 2-D flow past a rotating cylinder near an impermeable plane boundary has already been obtained by Liang and Liou (1995). However detailed two-dimensional Navier-Stokes simulations of the pump described above have been carried out by Sharatchandra et al. (1997a), who extended the operating range of Re beyond 100. The effects of varying the channel height H and the rotor eccentricity ϵ have been studied. It was demonstrated that an optimum plate spacing exists and that the induced flow increases monotonically with eccentricity; the maximum flow rate being achieved with the rotor in contact with a channel wall. Both the experimental results of Sen et al. (1996) and the 2-D numerical simulations of Sharatchandra et al. (1997a) have verified that the pump characteristics are linear and therefore kinematically reversible. Sharatchandra et al. (1997a; 1997b) also investigated the effects of slip flow on the pump performance as well as the thermal aspects of the viscous device.

In an actual implementation of the micropump,[2] both the rotor and the channel have a finite, in fact rather small, width. The principal objective of the present study is to consider what changes to the pump performance are brought about as the width of the channel becomes exceedingly small. It is anticipated that the bulk flow generated by the pump will decrease as a result of the additional resistance to the flow caused by the side

[2]Several other practical obstacles need to be considered but are not covered in here. Among those are the larger friction/stiction and seal design associated with rotational motion of microscale devices.

walls. However, the importance of this decrease and its effects on the operational envelope of the micropump remain to be detailed.

The second aim of this study is to describe the possible utilization of the inverse device as a turbine. The most interesting application of such a microturbine would be as a microsensor for measuring exceedingly small flow rates of the order of nanoliters/s (i.e., microflow metering for medical and other applications). Such microdosage (Gass et al., 1993; Lammerink et al., 1993) could be delivered, for example, by operating a micropump such as described above for only a finite number of turns or even a portion of a turn to displace a prescribed volume of fluid.

For both the pump and turbine configurations, a finite-element approach is used here to solve the corresponding three-dimensional Navier-Stokes equations. The numerical simulations document the influence of the channel width and height and rotor eccentricity on the pump-generated net flow in the presence of an externally imposed pressure gradient, or on the turbine-generated net torque in the presence of an externally imposed bulk velocity.

2 Methodology

The three-dimensional Navier-Stokes equations are numerically integrated using the FIDAP finite-element program (Fluid Dynamics International, Inc., Evanston, Illinois). This general purpose program uses a Galerkin formulation and is particularly suited for the present low-Re, complex-geometry flow problem. Finite-element algorithms are generally easily adaptable to situations where the boundaries do not follow coordinate lines, such as the present configuration. For microscale applications, we are interested in low Reynolds numbers for which we do not expect hydrodynamic instabilities and can assume steady flow. However, the creeping-flow assumption is not made in the present computations, thus retaining the nonlinear terms in the momentum equations and allowing extension to higher

albeit still moderate Re. The governing equations describing the laminar, incompressible, steady flow of a fluid with constant properties may be expressed in coordinate invariant dimensionless form as

$$\nabla.\mathbf{V} = 0 \tag{1}$$

$$\nabla.\left(\mathbf{VV} - \frac{1}{Re}\nabla\mathbf{V}\right) + \nabla p = 0 \tag{2}$$

where $\mathbf{V}$ is the dimensionless velocity vector and p is the dimensionless pressure. Gravity and other body forces are neglected. Here, the length scale is the cylinder diameter $D = 2\,a$, and the velocity scale is the prescribed rotor surface speed $U = \omega\,a$ for the pump problem or the prescribed bulk velocity $U = \bar{U}$ for the turbine problem. The Reynolds number is defined as $Re = U\,D/\nu$, where ν is the kinematic viscosity of the fluid. Pressure is normalized with respect to $\rho\,U^2$, where ρ is the fluid density. No-slip and no-penetration conditions are assumed to hold for the tangential and normal velocity components at a solid surface.

The load on the pump section is characterized by a pressure rise. Since this is an externally imposed quantity it is better to nondimensionalize it with respect to a quantity that is not dependent on the pump/turbine rotation. So we choose to scale it with $\rho\,\nu^2/4\,a^2$, instead of $\rho\,U^2$, and denote the dimensionless pressure rise by Δp^*. The ratio of these two pressure scales is, of course, Re^{-2}.

2.1 Problem Geometry

The geometry of the problem is described in Figure 1. The plane A (top) is positioned at a vertical distance h from the plane B (bottom). The cylindrical rotor is placed at distances h_U and h_L from the plates A and B, respectively. The distance between the two side walls C and D is w. The length l of the channel is taken equal to 16 times the diameter

of the cylinder, adequate to establish fully-developed flow far upstream and far downstream of the rotor (Sharatchandra et al., 1997a). The rotor is located halfway down the channel length and rotates clockwise with an angular velocity ω. The plane equidistant from C and D is a symmetry plane for the present flow.

The following dimensionless parameters are defined

$$H = \frac{h}{2a} \;\; ; \;\; W = \frac{w}{2a} \;\; ; \;\; L = \frac{l}{2a} \tag{3}$$

$$\epsilon = \frac{h_U + a - h/2}{2a} = \frac{h/2 - a - h_L}{2a} \tag{4}$$

where ϵ is the rotor eccentricity. When $\epsilon = 0$, the horizontal walls are equally spaced from the rotor, and when ϵ reaches its extreme values, the rotor is in contact with either of the plates. A dimensionless bulk velocity is defined by

$$\bar{u} = \frac{\bar{U}}{\omega\, a} \tag{5}$$

where $\bar{U}$ is the bulk velocity in the channel, which is to be computed for the pump problem but is prescribed for the turbine problem.

In nearly all the simulations, the Reynolds number is taken equal to 1. For glycerin as the working fluid and a cylinder radius of $a = 0.45$ cm, for example, this fixes the rotor surface speed at $\omega\, a = 13.17$ cm/s. In most of the cases $\Delta p^* = 1$, which means that $P_2 - P_1 = 21.85$ N/m^2, where the subscripts 1 and 2 refer to, respectively, the inlet and outlet of the duct. As was shown in the two-dimensional simulations of Sharatchandra et al. (1997a), slip-flow effects become significant only when the Knudsen number exceeds 0.01. Such effects are not considered here, implying an operating range of $Kn < 0.01$.

2.2 Grid Generation and Boundary Conditions

The accuracy and cost-effectiveness of the numerical simulations are to a large extent dependent on the finite-element mesh discretization employed. FIDAP mesh generator

FIMESH allows the creation of three-dimensional meshes in a semi-automatic way. The particular geometry of the present problem makes possible the generation of the mesh in the following cost-effective way. The mesh is created on the side wall C as if it was a 2-D mesh. FIMESH requires the subdivision of the face into domains that are topologically equivalent to rectangles. Once the mesh of this face is obtained and the number of elements in the third dimension is specified, FIMESH creates the quadrilaterals elements by projection of the 2-D mesh in the z-axis, resulting in a regular mesh in the spanwise direction.

At that point, a strategy of meshing is necessary. The idea is to distribute the nodal points according to the anticipated field variables. For large gradients in the field variables, the nodal points should be dense; and, for small gradients, the nodal points should be sparse. Therefore, it is necessary to make an estimate of how the field variables change in different regions of the problem domain when generating a mesh. For the pump problem, it is possible to use the results of the 2-D study of Sharatchandra et al. (1997a) to anticipate the regions with high gradients. In any case, it seems obvious that these regions will be close to the cylinder and the narrower gap, whereas regions near the inlet and outlet will have low gradients. FIMESH allows the generation of the boundary edges of the mesh with the desired spacing of nodal points by using line, circular arc or spline generators and then using surface and volume generators which preserve this spacing. When boundaries change drastically, the domain being modeled can be broken into multiple regions. Figure 2 gives an example of the kind of mesh which is used for the present simulations. The number of nodes which led to grid-independent computations was typically $120 \times 60 \times 16$. Note in particular the denser mesh in the vicinity of regions of anticipated high velocity gradients. When the cylinder is particularly close to one of the walls, a denser mesh is necessary so that the simulation converges in a reasonable number of steps.

The boundary condition specifications take advantage of the symmetry of the problem. A simulation is only made on a semi-channel limited on one side by a side wall and on the other side by the symmetry plane. For the pump problem, the boundary conditions are the following:

Symmetry plane :	$U_z = 0$	
Top, bottom and side :	$U_x = 0$	
	$U_y = 0$	
	$U_z = 0$	
Inlet and outlet :	$U_y = 0$	
	$U_z = 0$	
	$(P_2 - P_1)$	Prescribed
Cylinder :	U_{T1}	Prescribed
	$U_{T2} = 0$	
	$U_N = 0$	

where U_{T1}, U_{T2}, and U_N are the tangential and normal velocities on the cylinder; U_{T1} is the tangential velocity in the x-y plane, while U_{T2} is the one parallel to the z-axis.

In the case of the turbine, the boundary conditions are the same for the symmetry plane, the top, the bottom, the side and the cylinder, although U_{T1} is unknown in this case. For the inlet and the outlet, the conditions are as follow:

Inlet and outlet :	$U_y = 0$
	$U_z = 0$
	$U_x = \frac{4\,h^2}{\mu\,\pi^3}\,\left(-\frac{\mathrm{dP}}{\mathrm{dx}}\right)$
	$\sum_{i=1,3,5,\ldots}^{\infty}(-1)^{(i-1)/2}\,\left[1 - \frac{cosh(i\pi z/h)}{cosh(i\pi w/2h)}\right]\,\frac{cos(i\pi y/h)}{i^3}$

The above expression for U_x is the fully-developed velocity in a channel without obstacles and with a rectangular cross-section (White, 1991). The pressure gradient in this equation can be written in terms of the prescribed bulk velocity, $\bar{U}$, by simply integrating the inlet streamwise velocity distribution across the cross-sectional area. The resulting equation

reads

$$\left(-\frac{\mathrm{d}P}{\mathrm{d}x}\right) = \frac{12\,\mu\,\bar{U}}{h^2}\left[1 - \frac{192\,h}{\pi^5\,w}\sum_{i=1,3,5,\ldots}^{\infty}\frac{\tanh(i\pi w/2h)}{i^5}\right]^{-1} \tag{6}$$

A segregated solution algorithm has been designed to address large-scale simulations and is used in the present computations. The algorithm is essentially based on the implicit approach. Its principal characteristic is that it avoids the formation of a global system matrix which represents the global discretized matrix problem resulting from the application of the Galerkin finite-element method to the continuum flow equations. Instead, this matrix is decomposed into smaller sub-matrices each governing the nodal unknowns associated with only one conservation equation. These smaller sub-matrices are then solved in a sequential manner using conjugate gradient-type schemes. As the storage required for the individual sub-matrices is considerably less than that needed to store the global system matrix, the storage requirements of the segregated approach are substantially less than that of a fully-coupled approach.

3 Validation of the Simulation

For relatively long rotor (deep channel), the present three-dimensional computations should approach those of the 2-D simulations and the long-cylinder experiments of, respectively, Sharatchandra et al. (1997a) and Sen et al. (1996). Sharatchandra et al. had validated their own computational method against the analytical Wannier's (1950) solution for the flow between two eccentric cylinders as well as against the numerical simulations of Ingham (1983), Badr et al. (1989) and Ingham and Tang (1990) for the problem of a uniform viscous flow past a rotating cylinder. Indeed, when the dimensionless width W of the channel is larger than 20, the influence of the side walls is weaker and the present 3-D results approach those of the 2-D simulations as well as the experiments of Sen et al.

(1996).

Comparison between the 2-D and 3-D simulations for the pump is shown in the table below. The bulk velocity, which is obtained by dividing the flow rate by the cross-sectional area of the duct for the 3-D case or by h for the 2-D case, is compared for different values of the channel height and the rotor eccentricity. All quantities in this table are dimensionless and the 3-D channel width is 20 times the rotor diameter. At this relatively large aspect ratio, the flow field is nearly (but not quite) two-dimensional, as was found in our previous experiments (Sen et al., 1996). The present results indicate that the 3-D bulk velocities are, as expected, consistently below those for the 2-D computations, to within 5%. The cases where the eccentricity approaches its maximum values are the most difficult because in the infinitely thin space between the cylinder and the lower wall the velocity gradients are rather extreme. As already mentioned, a correspondingly fine mesh is needed in this region for fast convergence.

H	2.5	2.5	2	1.5	1.1
ϵ/ϵ_{max}	0.7	0.9	0.9	0.9	0.9
$\bar{u}_{2-D}$	0.0609	0.0698	0.0874	0.1023	0.0497
$\bar{u}_{3-D}$	0.0589	0.0679	0.0856	0.0973	0.0496

4 Results for the Pump Problem

All the results displayed in this paper are in the form of continuous lines obtained by simply joining the calculated data points. Typically, each curve consisted of 20–30 discrete points, and no curve fitting was necessary due to the closeness of the discrete points.

4.1 Three-Dimensional Effects on the Bulk Velocity

In a Stokes flow, the bulk velocity is proportional to the angular velocity of the cylinder. This has been demonstrated in the experiments of Sen et al. (1996) and the 2-D

numerical simulations of Sharatchandra et al. (1997a). A comparison between the 2-D and 3-D computations is depicted in Figure 3 for a channel height of $H = 2.5$, rotor eccentricity of $\epsilon/\epsilon_{max} = 0.9$, and global pressure gradient of $\Delta p^* = 0$. The dimensionless duct width for the 3-D case is $W = 0.6$. These geometric parameters correspond to an actual 3-D micropump which is currently under construction. The range of Re in the abscissa is between 0–1, and the depicted relation between the bulk velocity and rotor speed is linear for both the 2-D and 3-D cases. The resulting (dimensional) bulk velocity is 9% of the rotor surface speed for the 2-D case, while this constant of proportionality drops to 1% for the narrow duct.

The effect of varying the channel width on the resulting bulk velocity is shown in Figure 4. Here the operating parameters are:[3] $Re = 1$, $H = 2.5$, $\epsilon/\epsilon_{max} = 0.75$, and $\Delta p^* = 1$. The 3-D results asymptotically approach the 2-D value of $\bar{u} = 0.06$ for $W > 20$, and the bulk velocity monotonically decreases as the two side walls become closer. The change is gradual at first but accelerates once the dimensionless channel width drops below about 5. The presence of the side walls causes an increase in the viscous resistance to the flow and a subsequent decrease in the bulk velocity. At $W = 0.6$, the bulk velocity is only 10% of that for the infinitely wide channel. The inset in Figure 4 shows the behavior for very narrow channels. The presence of a global adverse pressure gradient combined with an increase in viscous losses cause a reverse flow for $W < 0.18$ but the amplitude of this reverse flow gradually diminishes to zero as the two side walls eventually touch. The global reverse flow disappears altogether when the global pressure gradient is zero or favorable.

We next look at the effects of changing the channel height and rotor eccentricity on the bulk velocity. For these simulations the Reynolds number and the pressure gradient

[3] As a reminder, Re for the pump is defined in terms of the rotor diameter and its surface speed.

are both fixed at $Re = 1$ and $\Delta p^* = 1$. Figure 5 shows $\bar{u} = f(H)$ for several values of W, where ϵ/ϵ_{max} is fixed and equal to 0.9. Again, as the channel narrows, less bulk velocity is generated by the rotation of the rotor. The curves in this figure maintain their general shape as the distance between side walls, W, diminishes; the bulk velocity drops to zero for upper and lower wall separations which are either too large or too small. In between these too extremes, there is an optimum channel height. It is interesting to note that the different curves collapse for dimensionless channel heights lower than about 1.1. It appears that in this case the duct width has diminished effect on the bulk velocity; the flow is mainly influenced by the upper and lower walls separation.

An optimum channel height which gives the maximum flow rate for a given rotor surface speed is observed, as was the case for the two-dimensional case ($W = \infty$). However, the optimum H gradually shifts to the left as the duct narrows. This trend is clearly depicted in Figure 6; optimum H being 1.5 for the 2-D channel, and decreases to approximately 1.15 as the two side walls touch.[4]

The curves $\bar{u} = f(\epsilon/\epsilon_{max})$, where H is maintained constant at 2.5, are depicted in Figure 7. At a particular channel width and for the range of eccentricities investigated here, $\bar{u}$ increases monotonically with ϵ/ϵ_{max}. This was the case also for the 2-D simulations where the bulk velocity reached its highest value when the eccentricity was a maximum, that is to say when the cylinder was in contact with either the lower or upper wall. The curvature of the curves changes sign for values of $W > 2$, but the reason for this is not presently understood. At low values of eccentricity, a reverse flow is observed as a result of the imposed adverse pressure gradient. The magnitude of this reverse flow is diminished as the two side walls become closer; the additional resistance caused by the side walls has

[4]The value 1.15 results from extrapolating the curve in Figure 6 to $W = 0$.

a similar detrimental effect on both the forward and reverse flows. It is interesting to note that, for all values of channel width, the onset of reverse flow occurs at about the same value of relative eccentricity of $\epsilon/\epsilon_{max} \approx 0.1$.

4.2 Three-Dimensional Effects on the Pump Performance

In this subsection, we investigate the effects of the side walls on the pump characteristics and coefficient of performance. The Reynolds number is held constant in all the runs at $Re = 1$. For creeping flows, the flow rate (or bulk velocity) are expected to vary linearly with the imposed pressure gradient. This has been analytically demonstrated by Sharatchandra et al. (1997a) for the two-dimensional viscous pump. That trend holds for 3-D pumps as well, as shown in Figure 8. Here, $H = 2.5$ and $\epsilon/\epsilon_{max} = 0.7$. The slope of the straight lines diminishes as the duct width is reduced, but all lines intersect the abscissa at the same Δp^* of 4. This is the pressure gradient at which the pump yields zero bulk velocity. At higher adverse pressure gradients, the mean flow in the channel is reversed. At zero pressure gradient, a narrow duct leads to lower bulk velocity consistent with the results of Section 4.1.

A measure of the viscous pumping efficiency is given by the ratio of the useful flow power produced to the input energy to the pump. An energy balance shows this coefficient of performance to be

$$\eta = \frac{H\ \bar{u}\ \Delta p^*}{Re^2\ \ C_M} \tag{7}$$

where C_M is the moment coefficient obtained by integrating the viscous shear stress around the rotor

$$C_M = \frac{1}{w} \int_{-w/2}^{w/2} \int_0^{2\pi} \tau \ \mathrm{d}\theta \ \mathrm{d}z \tag{8}$$

where τ is the shear stress normalized with $\rho\, U^2$.[5]

Figure 9 shows the effect of channel width on the pump coefficient of performance, for $Re = 1$, $H = 2.5$, $\epsilon/\epsilon_{max} = 0.7$, and $\Delta p^* = 1$. Narrow channels lead to lower pump efficiency due to the additional viscous losses caused by the side walls. This effect accelerates for values of W lower than 5, consistent with the lower bulk velocity observed in Figure 4. The efficiency is below 1% even for the two-dimensional pump as was observed by Sharatchandra et al. (1997a). This is caused by the very high rates of dissipation intrinsic to the operation of a viscous pump. As the channel narrows, an increasingly large portion of the shear work imparted to the fluid by the rotor is dissipated into heat, and the pumping efficiency correspondingly drops.[6]

It is relevant to note that C_M is only a weak function of Δp^* for fixed values of H and ϵ. This is because, close to the rotor surface, the flow structure is dictated by the shearing action of the rotating cylinder, rather than by the externally imposed pressure gradient. Consequently, the shear stress distribution is more or less the same for all values of Δp^*. Since C_M is almost a constant, close inspection of Equation (7) indicates that, for a given Re, H and ϵ/ϵ_{max}, the η vs. Δp^* curve should be almost parabolic, as was shown for the 2-D case by Sharatchandra et al. (1997a). The most efficient pump performance is thus obtained for $\Delta p^* \approx \Delta p_0^*/2$, where Δp_0^* is the adverse pressure gradient at which the bulk velocity changes sign and the pump efficiency becomes zero.

The three-dimensional pump behaves qualitatively in a similar manner as indicated in Figure 10, for $Re = 1$, $H = 1.5$, and $\epsilon/\epsilon_{max} = 0.9$. The coefficient of performance is generally higher for this higher-eccentricity, lower-channel-height case. But once again, the

[5]Note that Re will not explicitly appear in Equation (7) if the pressure and shear stress are normalized using the same viscous scale.

[6]The proportion of fluid affected by the side-wall viscous layer is obviously increased as the channel narrows.

narrow channel ($W = 0.6$) leads to lower efficiency as compared to the 2-D pump ($W = \infty$). Moreover, the maximum efficiency for the three-dimensional pump occurs at slightly higher pressure gradient. Note that, for the present high eccentricity configuration, Δp_0^* is different for the 2-D and 3-D channels, whereas for the lower eccentricity case depicted in Figure 8, Δp_0^* was the same for all channel widths. It appears that, as the two side walls close on a highly eccentric rotor, higher adverse pressure gradients are needed before the pump *stalls*.

5 Results for the Turbine Problem

The viscous pump described thus far operates at low Reynolds numbers and should therefore be kinematically reversible. A microturbine based on the same principle should, therefore, lead to a net torque in the presence of a prescribed bulk velocity. The results of three-dimensional numerical simulations of the envisioned microturbine are described in this section. As already stated in Section 2, the Reynolds number for the turbine problem is defined in terms of the bulk velocity, since the rotor surface speed is unknown in this case

$$Re = \frac{\bar{U}\,(2a)}{\nu} \tag{9}$$

Figure 11 shows the dimensionless rotor speed as a function of the bulk velocity, for $W = \infty$ and $W = 0.6$. In these simulations, $H = 2.5$ and $\epsilon/\epsilon_{max} = 0.9$. The relation is linear as was the case for the pump problem (Figure 3). The slope of the lines is 0.37 for the 2-D turbine and 0.33 for the narrow channel with $W = 0.6$. This means that the induced rotor speed is, respectively, 0.37 and 0.33 of the bulk velocity in the channel.[7] For the pump, the corresponding numbers were 11.11 for the 2-D case and 100 for the 3-D case. Although it appears that the side walls have bigger influence on the pump performance, it should be

[7]The rotor speed can never, of course, exceed the fluid velocity even if there is no load on the turbine. Without load, the integral of the viscous shear stress over the entire surface area of the rotor is exactly zero, and the turbine achieves its highest albeit finite rpm.

noted that in the turbine case a vastly higher pressure drop is required in the 3-D duct to yield the same bulk velocity as that in the 2-D duct ($\Delta p^* = -29$ versus $\Delta p^* = -1.5$).

The turbine characteristics are depicted in Figure 12, for $H = 2.5$ and $\epsilon/\epsilon_{max} = 0.9$. A turbine load results in a moment on the shaft, which at steady state balances the torque due to viscous stresses. The dimensionless rotor speed is plotted versus the moment coefficient for $W = \infty$ and $W = 0.6$. This figure is analogous to Figure 8 for the pumping device. In here, the bulk velocity is fixed at $Re = 0.01$, and the rotor speed is determined for different loads on the turbine. Again, the turbine characteristics are linear, but the side walls have weaker, though still adverse, effect on the device performance as compared to the pump case. At large enough loads ($C_M > 4$), the rotor will not spin, and maximum rotation is achieved when the turbine is subjected to zero load.

6 Conclusions

In this paper, we have investigated end-wall effects on the performance of a novel pump/turbine device appropriate for microscale and other low-Reynolds-number applications. The three-dimensional Navier-Stokes equations have been numerically integrated using a finite-element approach to document the flow field and to determine the turbomachine characteristics and efficiency. A rotor eccentrically placed within a 3-D duct has been shown to be capable of generating a net flow against an externally imposed pressure gradient, or, as a turbine, generating a net torque in the presence of a prescribed bulk flow.

The numerical simulations indicate a gradual deterioration of the pump performance as the two side walls become closer providing increased viscous resistance to the flow. However, effective pumping is still observed within channels whose widths are only a fraction of the rotor diameter. An optimum channel height still exists in the 3-D case, although this height decreases as the channel narrows. The highest bulk velocity is achieved when the rotor is

in contact with either the lower or upper wall.

At low Reynolds numbers, the 3-D pump characteristics are linear as was the case for the two-dimensional version. A parabolic relation between the pump efficiency and the imposed pressure gradient has been verified. The efficiency of the 3-D pump is, however, lower than that of its 2-D counterpart.

The utility of the envisioned viscous device as microturbine has been demonstrated for the first time in the present simulations. In this mode, the low-Reynolds-number turbine could be used as a microsensor for measuring exceedingly small flow rates, of the order of nanoliters/s. The turbine characteristics are also linear in the Stokes flow regime. The rotor speed is proportional to the imposed bulk velocity, but the constant of proportionality is slightly lower for the 3-D case. For a given bulk velocity, the rotor speed drops linearly as the external load on the turbine increases.

Actual implementation of the envisioned pump/turbine device for MEMS and other low-Reynolds-number applications should prove useful for a variety of fields including the delivery and metering of medical microdosages and the hauling of highly-viscous polymers. Construction of proper prototypes at the microscale should prove highly desirable to answer many practical questions related to eventual usage of the micropump and microturbine.

Acknowledgments

This study was performed under a contract from the National Science Foundation, under the Small Grants for Exploratory Research initiative (SGER Grant No. CTS-95-21612). The technical monitor is Dr. Roger E. A. Arndt. The authors are grateful to Dr. M.C. Sharatchandra who supplied us with the results of the two-dimensional simulations.

REFERENCES

Angell, J.B., Terry, S.C., and Barth, P.W. (1983) "Silicon Micromechanical Devices," *Scientific American*, vol. 248, April, pp. 44–55.

Badr, H.M., Dennis, S.C.R., and Young, P.J.S. (1989) "Steady and Unsteady Flow Past a Rotating Cylinder at Low Reynolds Numbers," *Computers and Fluids*, vol. 17, pp. 579–609.

Bart, S.F., Tavrow, L.S., Mehregany, M., and Lang, J.H. (1990) "Microfabricated Electrohydrodynamic Pumps," *Sensors and Actuators A*, vol. 21-23, pp. 193–197.

Esashi, M., Shoji, S., and Nakano, A. (1989) "Normally Closed Microvalve Fabricated on a Silicon Wafer," *Sensors and Actuators*, vol. 20, pp. 163–169.

Fuhr, G., Hagedorn, R., Müller, T., Benecke, W., and Wagner, B. (1992) "Microfabricated Electrohydrodynamic (EHD) Pumps for Liquids of Higher Conductivity," *Journal of Micro Electro Mechanical Systems*, vol. 1, pp. 141–145.

Gabriel, K.J. (1995) "Engineering Microscopic Machines," *Scientific American*, vol. 273, September, pp. 150–153.

Gabriel, K.J., Jarvis, J., and Trimmer, W. (editors) (1988) "Small Machines, Large Opportunities: A Report on the Emerging Field of Microdynamics," National Science Foundation, published by AT&T Bell Laboratories, Murray Hill, New Jersey.

Gass, V., Van der Schoot, B.H., De Rooij, N.F., (1993) "Nanofluid Handling by Micro-Flow-Sensor based on Drag Force Measurements," *Journal of Micro Electro Mechanical Systems*, vol. 6, pp. 167–172.

Gravesen, P., Branebjerg, J., and Jensen, O.S. (1993) "Microfluidics—A Review," *Journal of Micromechanics and Microengineering*, vol. 3, pp. 168-182.

Hogan, H. (1996) "Invasion of the micromachines," *New Scientist*, vol. 29, June, pp. 28–33.

Ingham, D.B. (1983) "Steady Flow Past a Rotating Cylinder," *Computers and Fluids*, vol. 11, pp. 351–386.

Ingham, D.B., and Tang, T. (1990) "A Numerical Investigation into the Steady Flow Past a Rotating Circular Cylinder at Low and Intermediate Reynolds Numbers," *Journal of Computational Physics*, vol. 87, pp. 91-107.

Lammerink, T.S.J., Elwenspoek, M., Fluitman, J.H.J., (1993) "Integrated Micro-Liquid Dosing System," *Journal of Micro Electro Mechanical Systems*, vol. 6, pp. 254–259.

Liang, W.J., and Liou, J.A., (1995) "Flow Around a Rotating Cylinder Near a Plane Boundary," *Journal of the Chinese Institute of Engineers,* vol. 18, no. 1, pp. 35–50.

Lipkin, R. (1993) "Micro Steam Engine Makes Forceful Debut," *Science News*, vol. 144, p. 197.

Moroney, R.M., White, R.M., and Howe, R.T. (1991) "Ultrasonically Induced Microtransport," *Proceedings IEEE MEMS 91*, Nara, Japan, pp. 277–282, IEEE, New York.

O'Connor, L. (1992) "MEMS: Micromechanical Systems," *Mechanical Engineering*, vol. 114, February, pp. 40–47.

Odell, G.M., and Kovasznay, L.S.G. (1971) "A Water Pump with Density Stratification," *Journal of Fluid Mechanics,* vol. 50, pp. 535–557.

Richter, A., Plettner, A., Hofmann, K.A., and Sandmaier, H. (1991a) "Electrohydrodynamic Pumping and Flow Measurement," *Journal of Micro Electro Mechanical Systems*, vol. 4, pp. 271–276

Richter, A., Plettner, A., Hofmann, K.A., and Sandmaier, H. (1991b) "A Micromachined Electrohydrodynamic (EHD) Pump," *Sensors and Actuators A*, vol. 29, pp. 159–168.

Sen, M. , Wajerski , D., and Gad-el-Hak, M. (1996) "A Novel Pump for Low-Reynolds-Number Flows," *Journal of Fluids Engineering*, vol. 118, pp. 624–627.

Sharatchandra, M.C., Sen, M., and Gad-el-Hak, M. (1997a) "Navier-Stokes Simulations of a Novel Micropump," submitted to *ASME Journal of Fluids Engineering*, vol. 119, no. 2.

Sharatchandra, M.C., Sen, M., and Gad-el-Hak, M. (1997b) "Thermal Aspects of a Novel Viscous Pump," submitted to *ASME Journal of Heat Transfer*.

Smits, J.G. (1990) "Piezoelectric Micropump with Three Valves Working Peristaltically," *Sensors and Actuators A*, vol. 21-23, pp. 203–206.

Taylor, G. (1972) "Low-Reynolds-Number Flows," in *Illustrated Experiments in Fluid Mechanics*, pp. 47-54, National Committee for Fluid Mechanics Films, M.I.T. Press, Cambridge, Massachusetts.

Van Lintel, H.T.G., Van de Pol, F.C.M., and Bouwstra, S. (1988) "A Piezoelectric Micropump Based on Micromachining of Silicon," *Sensors and Actuators*, vol. 15, pp. 153–167.

Wannier, G.H. (1950) "A Contribution to the Hydrodynamics of Lubrication," *Quarterly of Applied Mathematics*, vol. 8, pp. 1–32.

White, F.M. (1991) *Viscous fluid flow*, second edition, McGraw-Hill, New York.

FIGURE LEGENDS

Fig. 1: Problem geometry.

Fig. 2: An example of computational mesh generation. For $H = 2.5$, $\epsilon/\epsilon_{max} = 0.9$, $W = 1$.

Fig. 3: Bulk velocity as a function of the rotor's radian velocity. For $H = 2.5$, $\epsilon/\epsilon_{max} = 0.9$, $\Delta p^* = 0$.

Fig. 4: Three-dimensional effects on the bulk velocity. For $Re = 1$, $H = 2.5$, $\epsilon/\epsilon_{max} = 0.75$, $\Delta p^* = 1$.

Fig. 5: Changes of the bulk velocity as a function of channel height, for several values of channel width. For $Re = 1$, $\epsilon/\epsilon_{max} = 0.9$, $\Delta p^* = 1$.

Fig. 6: Channel height necessary to generate peak bulk velocity, as a function of channel width. For $Re = 1$, $\epsilon/\epsilon_{max} = 0.9$, $\Delta p^* = 1$.

Fig. 7: Changes of the bulk velocity as a function of eccentricity, for several channel widths. For $Re = 1$, $H = 2.5$, $\Delta p^* = 1$.

Fig. 8: Pump characteristics for different channel widths. For $H = 2.5$, $\epsilon/\epsilon_{max} = 0.7$.

Fig. 9: Three-dimensional effects on the pump performance. For $Re = 1$, $H = 2.5$, $\epsilon/\epsilon_{max} = 0.7$, $\Delta p^* = 1$.

Fig. 10: Pump performance for two-dimensional and three-dimensional channels. For $Re = 1$, $H = 1.5$, $\epsilon/\epsilon_{max} = 0.9$.

Fig. 11: Turbine rotation as a function of the bulk velocity in the channel. For $H = 2.5$, $\epsilon/\epsilon_{max} = 0.9$.

Fig. 12: Turbine characteristics for two-dimensional and three-dimensional channels. For $H = 2.5$, $\epsilon/\epsilon_{max} = 0.9$.

Figure 1: Problem geometry.

Figure 2: An example of computational mesh generation. For $H = 2.5$, $\epsilon/\epsilon_{max} = 0.9$, $W = 1$.

Figure 3: Bulk velocity as a function of the rotor's radian velocity. For $H = 2.5$, $\epsilon/\epsilon_{max} = 0.9$, $\Delta p^* = 0$.

Figure 4: Three-dimensional effects on the bulk velocity. For $Re = 1$, $H = 2.5$, $\epsilon/\epsilon_{max} = 0.75$, $\Delta p^* = 1$.

Figure 5: Changes of the bulk velocity as a function of channel height, for several values of channel width. For $Re = 1$, $\epsilon/\epsilon_{max} = 0.9$, $\Delta p^* = 1$.

Figure 6: Channel height necessary to generate peak bulk velocity, as a function of channel width. For $Re = 1$, $\epsilon/\epsilon_{max} = 0.9$, $\Delta p^* = 1$.

Figure 7: Changes of the bulk velocity as a function of eccentricity, for several channel widths. For $Re = 1$, $H = 2.5$, $\Delta p^* = 1$.

Figure 8: Pump characteristics for different channel widths. For $H = 2.5$, $\epsilon/\epsilon_{max} = 0.7$.

Figure 9: Three-dimensional effects on the pump performance. For $Re = 1$, $H = 2.5$, $\epsilon/\epsilon_{max} = 0.7$, $\Delta p^* = 1$.

Figure 10: Pump performance for two-dimensional and three-dimensional channels. For $Re = 1$, $H = 1.5$, $\epsilon/\epsilon_{max} = 0.9$.

Figure 11: Turbine rotation as a function of the bulk velocity in the channel. For $H = 2.5$, $\epsilon/\epsilon_{max} = 0.9$.

Figure 12: Turbine characteristics for two-dimensional and three-dimensional channels. For $H = 2.5$, $\epsilon/\epsilon_{max} = 0.9$.

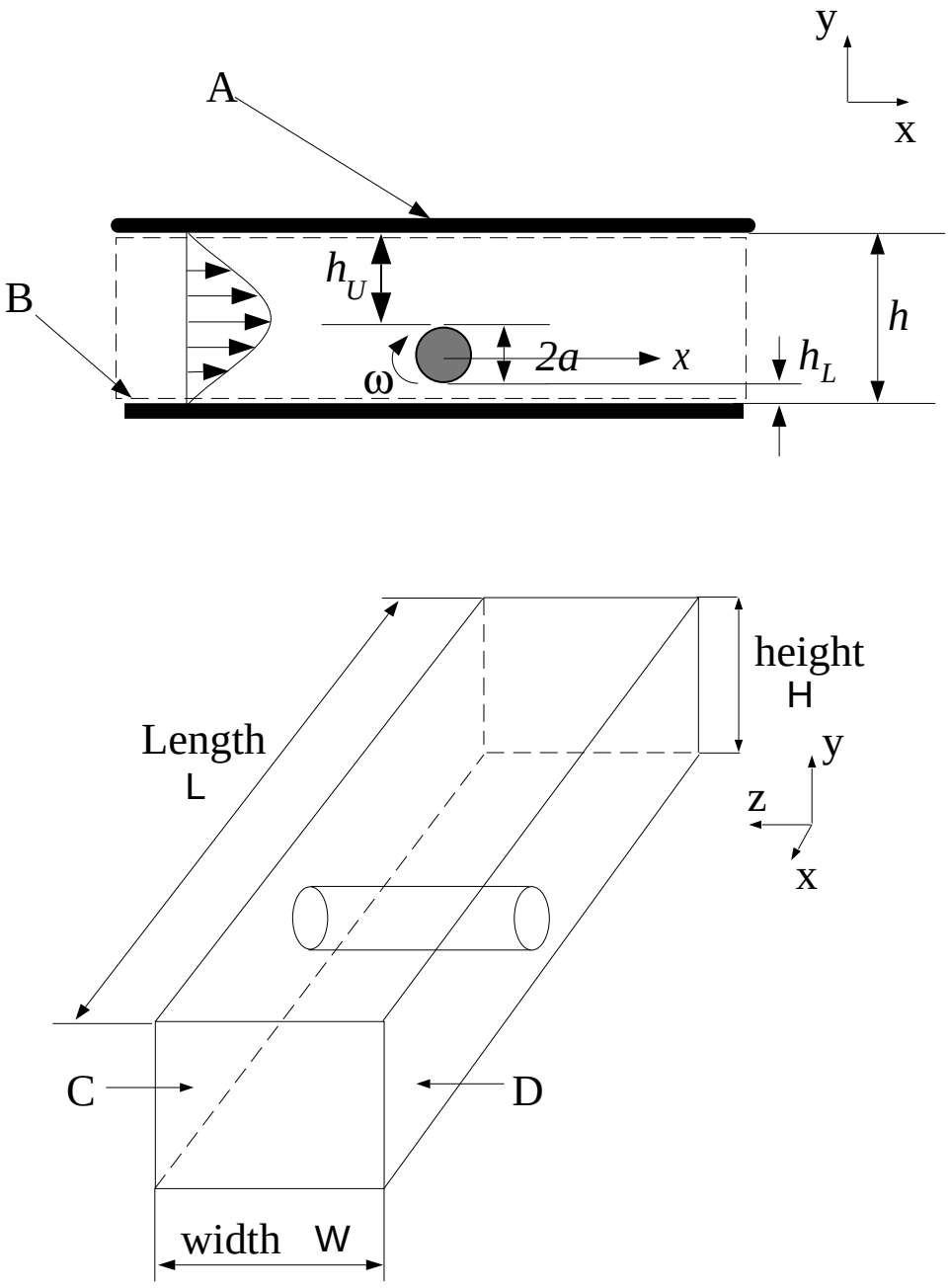

Figure 1: Problem geometry.

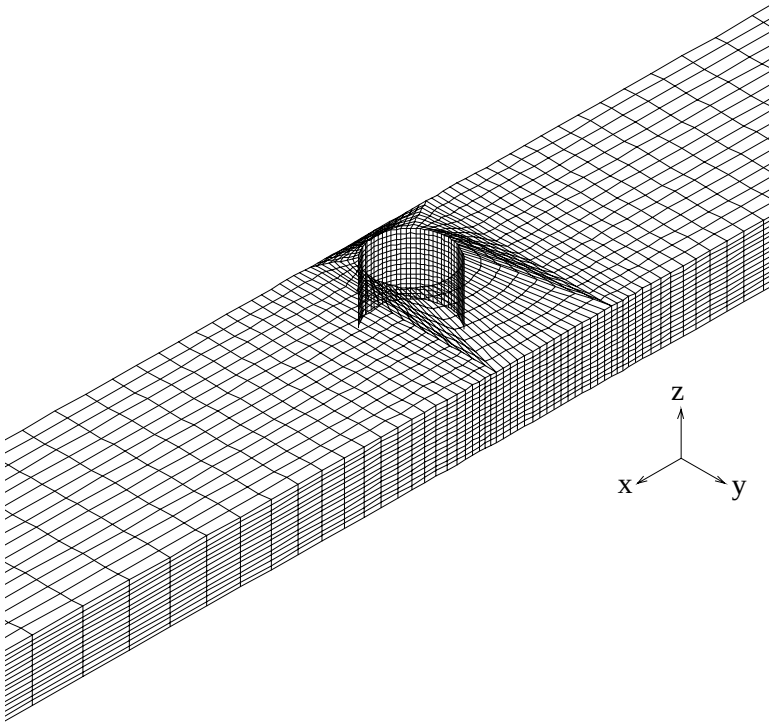

Figure 2: An example of computational mesh generation. For $H = 2.5$, $\epsilon/\epsilon_{max} = 0.9$, $W = 1$.

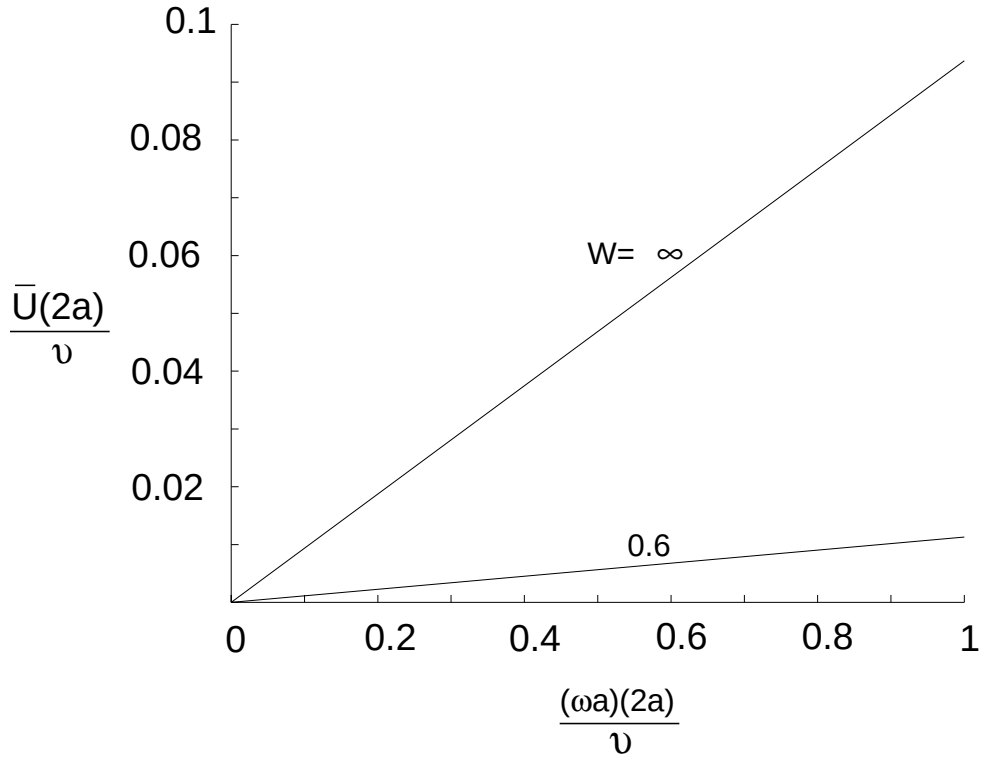

Figure 3: Bulk velocity as a function of the rotor's radian velocity. For $H = 2.5$, $\epsilon/\epsilon_{max} = 0.9$, $\Delta p^* = 0$.

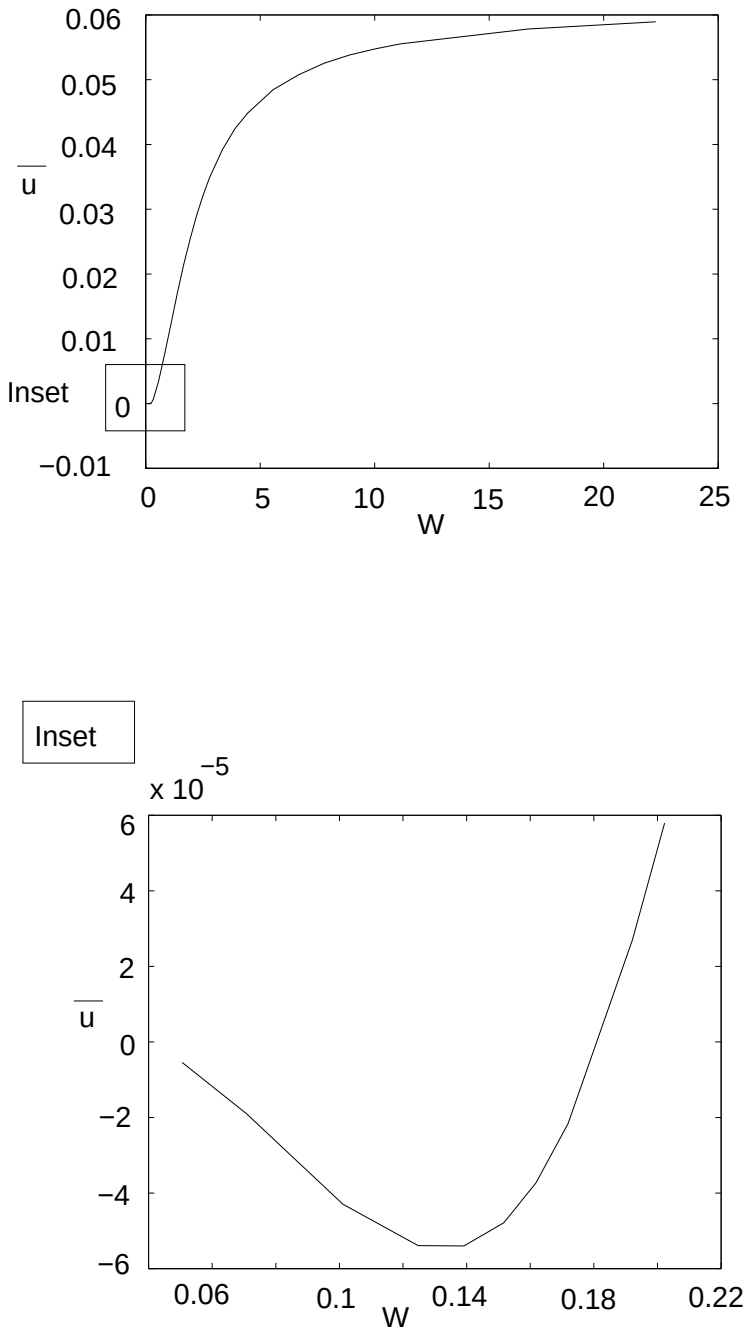

Figure 4: Three-dimensional effects on the bulk velocity. For $Re = 1$, $H = 2.5$, $\epsilon/\epsilon_{max} = 0.75$, $\Delta p^* = 1$.

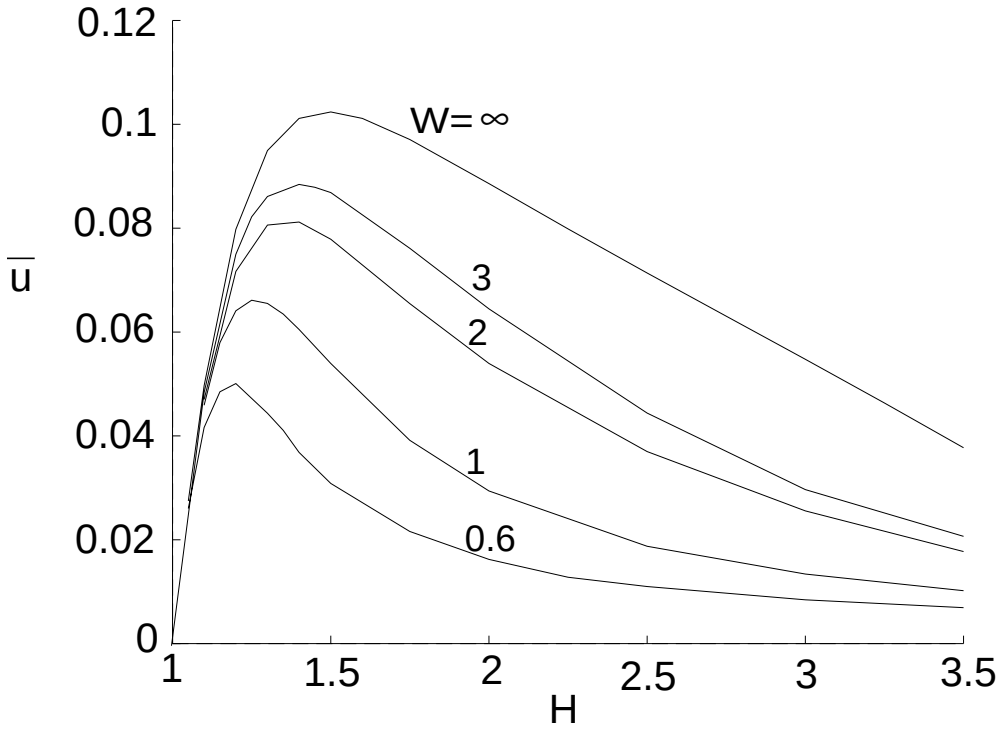

Figure 5: Changes of the bulk velocity as a function of channel height, for several values of channel width. For $Re = 1$, $\epsilon/\epsilon_{max} = 0.9$, $\Delta p^* = 1$.

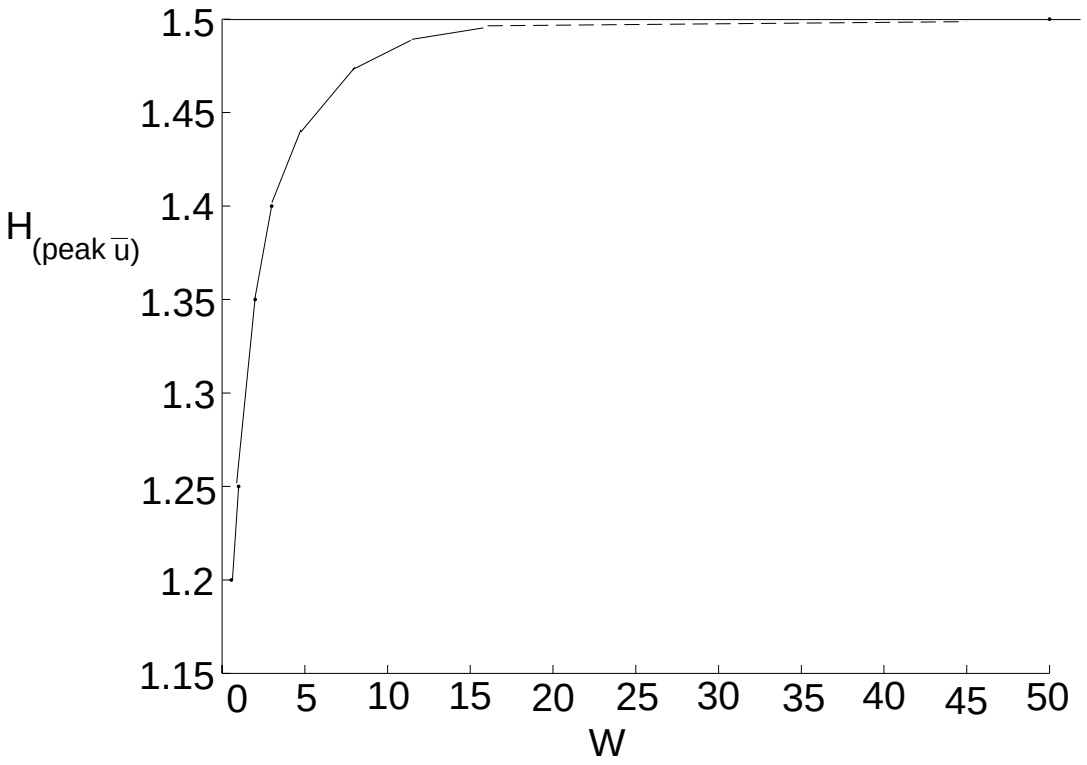

Figure 6: Channel height necessary to generate peak bulk velocity, as a function of channel width. For $Re = 1$, $\epsilon/\epsilon_{max} = 0.9$, $\Delta p^* = 1$.

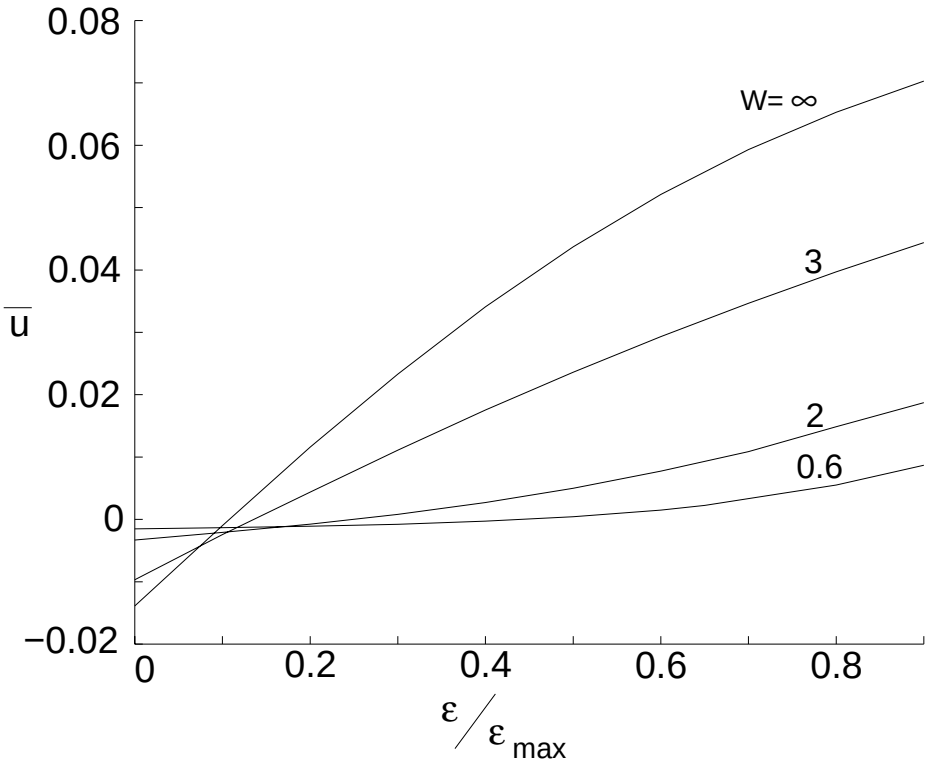

Figure 7: Changes of the bulk velocity as a function of eccentricity, for several channel widths. For $Re = 1$, $H = 2.5$, $\Delta p^* = 1$.

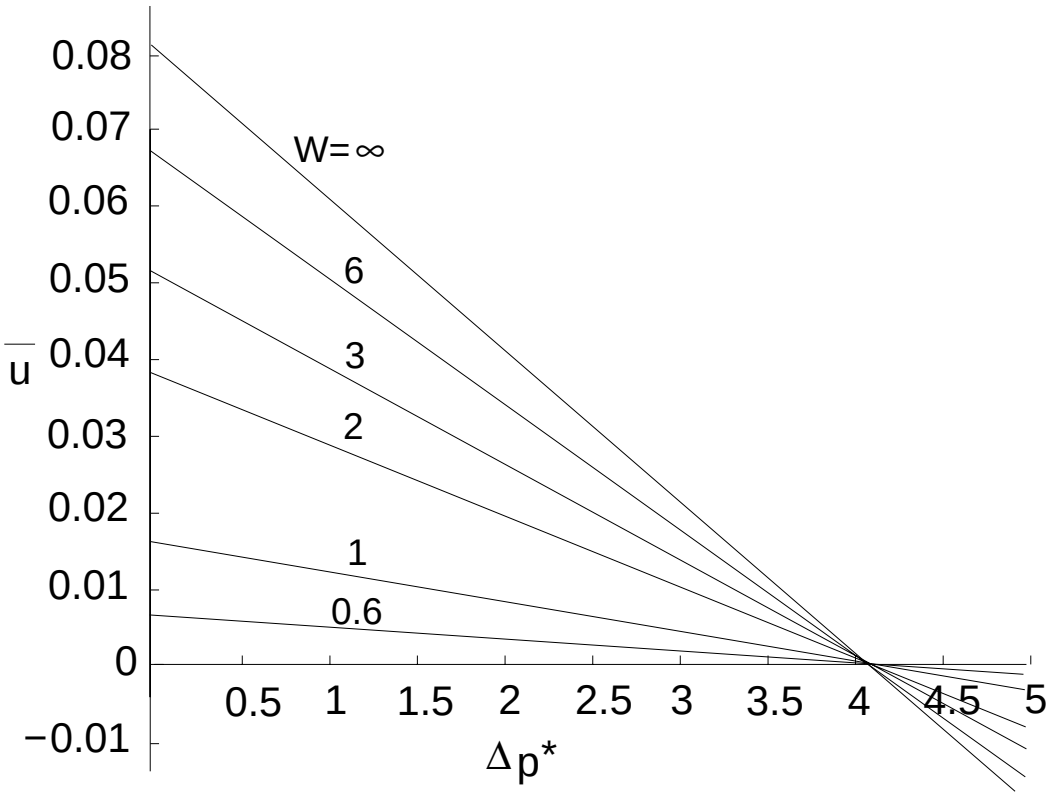

Figure 8: Pump characteristics for different channel widths. For $H = 2.5$, $\epsilon/\epsilon_{max} = 0.7$.

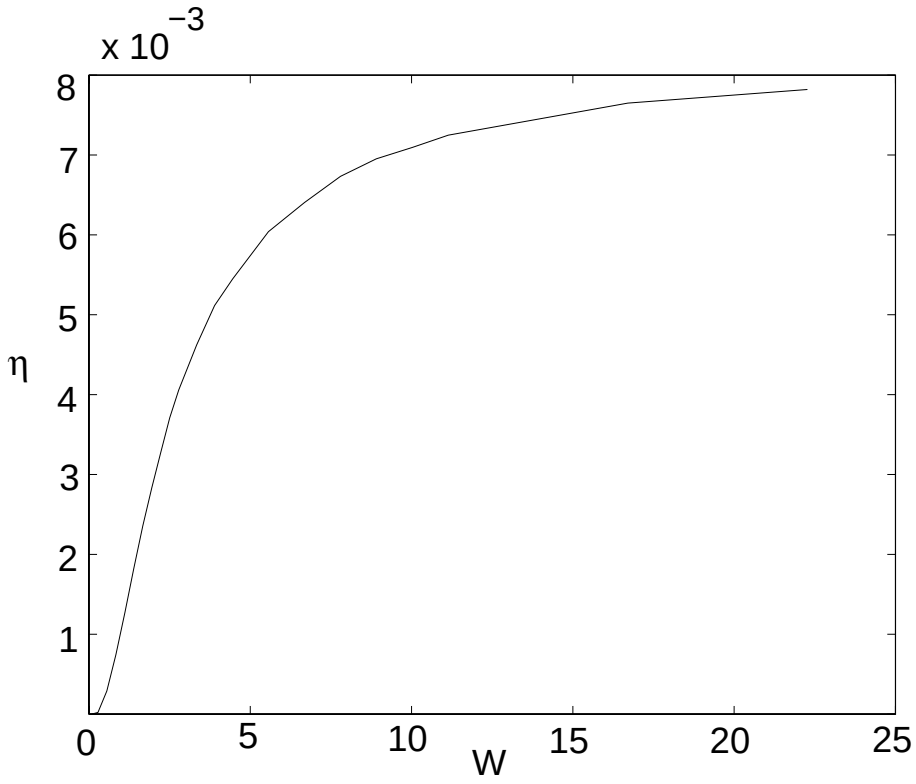

Figure 9: Three-dimensional effects on the pump performance. For $Re = 1$, $H = 2.5$, $\epsilon/\epsilon_{max} = 0.7$, $\Delta p^* = 1$.

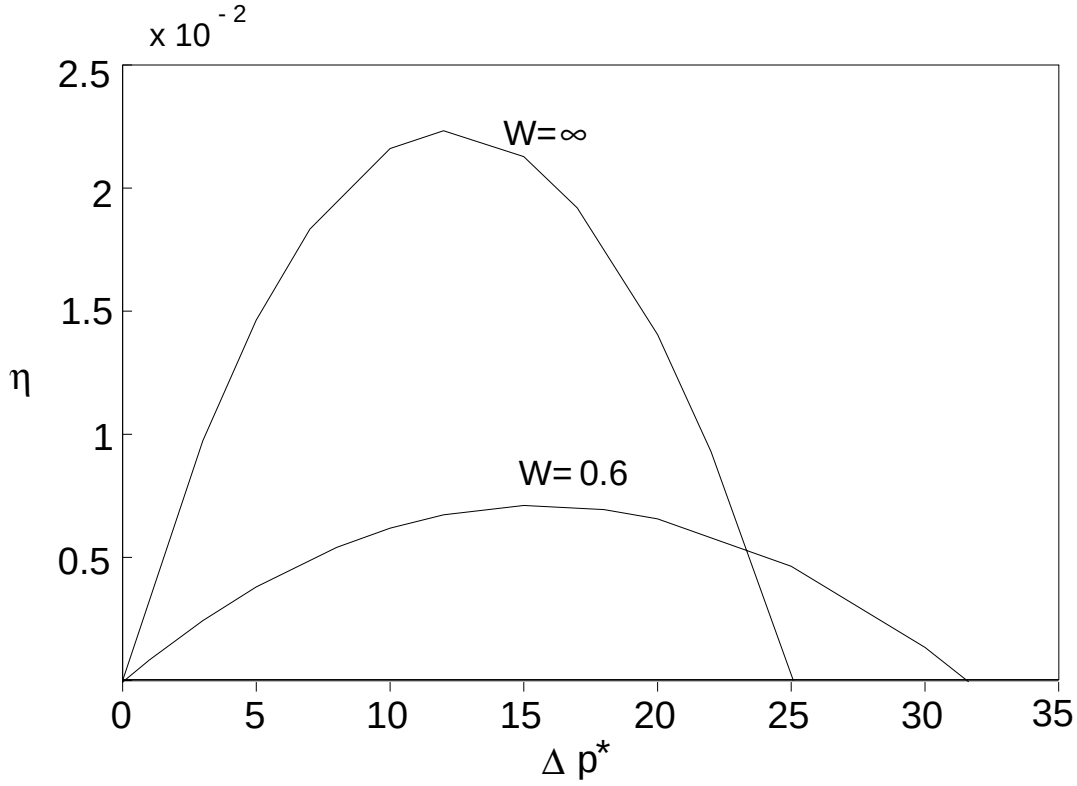

Figure 10: Pump performance for two-dimensional and three-dimensional channels. For $Re = 1$, $H = 1.5$, $\epsilon/\epsilon_{max} = 0.9$.

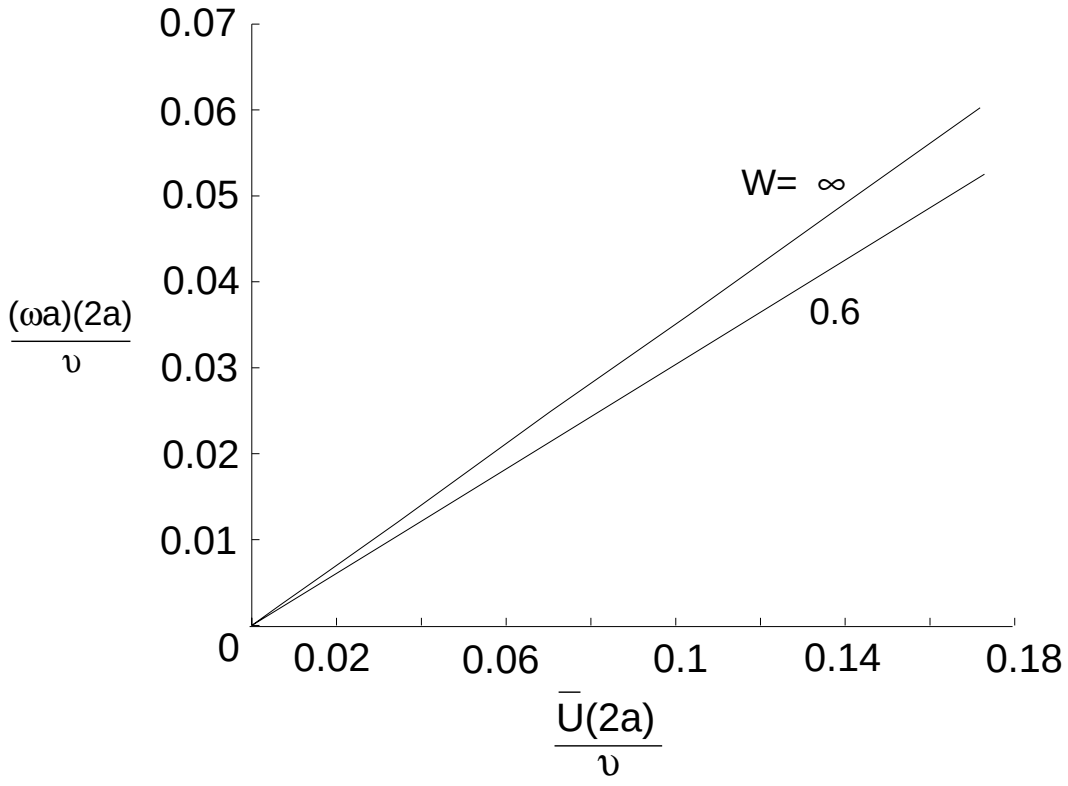

Figure 11: Turbine rotation as a function of the bulk velocity in the channel. For $H = 2.5$, $\epsilon/\epsilon_{max} = 0.9$.

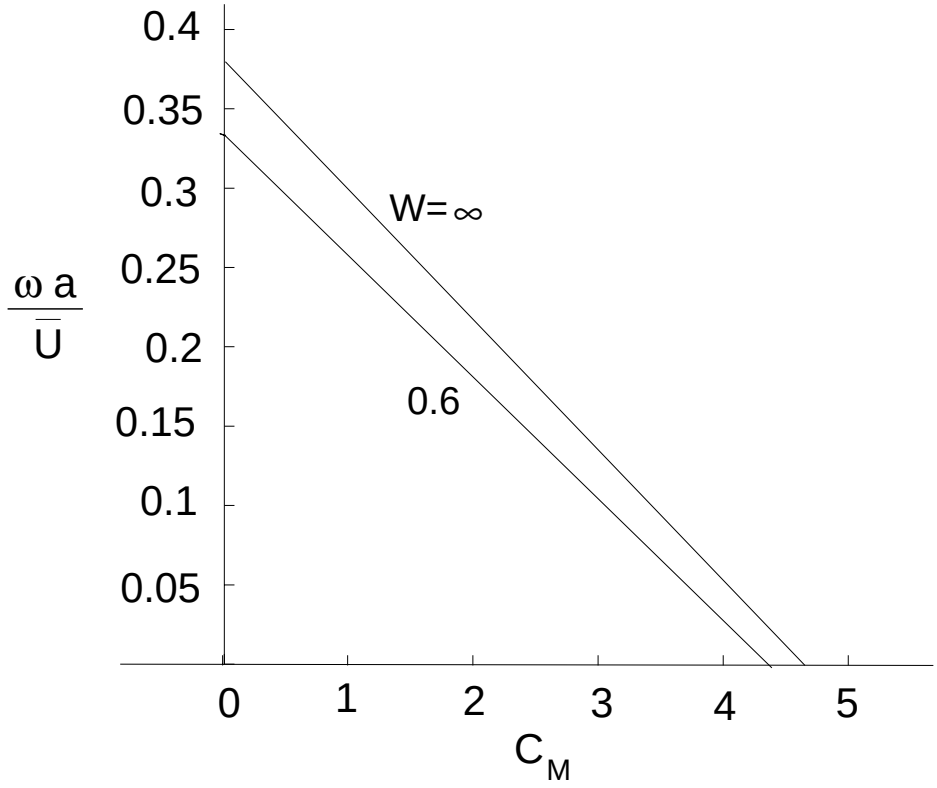

Figure 12: Turbine characteristics for two-dimensional and three-dimensional channels. For $H = 2.5$, $\epsilon/\epsilon_{max} = 0.9$.